JOURNAL OF AIRCRAFT
Vol. 46, No. 5, September–October 2009

Design and Testing of Multi-Element Airfoil for Short-Takeoff-and-Landing Ultralight Aircraft

D. P. Coiro,* F. Nicolosi,† and F. Grasso‡
University of Naples "Federico II," 80125 Napoli, Italy

DOI: 10.2514/1.43429

The design and analysis of a new airfoil to be employed on a ultralight aircraft with short takeoff and landing is presented. An inverse design philosophy has been applied and is described; the numerical analysis performed used XFOIL, MSES, and TBVOR computational codes and the effects of airfoil shape on complete aircraft performances were taken into account. A high-lift configuration, including slat and single-slotted flap geometries, has been developed and is illustrated in this paper. Exhaustive wind-tunnel tests were performed at the Department of Aerospace Engineering and the experimental results are described here. To validate numerical results and to analyze the effect of laminar bubbles on airfoil performance, the pressures on airfoil surface and in the wake were measured and flow visualizations were done using fluorescent oil. The landing configuration was also tested and an experimental optimization of flap and slat positions was carried out to obtain a high maximum lift coefficient.

Nomenclature

α	=	angle of attack
c	=	airfoil chord
$C_{D\text{eq}}$	=	complete aircraft trimmed drag coefficient
C_d	=	drag coefficient
$C_{d\,\min}$	=	airfoil minimum drag coefficient
$C_{L\text{eq}}$	=	complete aircraft trimmed lift coefficient
C_l	=	lift coefficient
$C_{l\,\max}$	=	maximum lift coefficient
$C_{\text{mc}/4}$	=	moment coefficient with respect to 25% of the chord
C_p	=	pressure coefficient
Lh	=	tail load
$\text{RC}_{\max}$	=	maximum rate of climb
$V_{\max}$	=	maximum speed
V_s	=	clean configuration stall speed
V_{sff}	=	full flap configuration stall speed

I. Introduction

THE design of a new STOL (short takeoff and landing) ultralight aircraft was carried out at the Department of Aerospace Engineering (DIAS) by the Aircraft Design and Aeroflightdynamics Group; a general view of the aircraft is shown in Fig. 1. The commercial success of the STOL aircraft depends mainly on the capability of combining good cruise performances with excellent short takeoff and landing. However, some STOL light aircraft with quite low maximum speed performances, such as the well-known Zenith CH701 (see Fig. 2), have received worldwide recognition, thus demonstrating that STOL capabilities can be a key to commercial success in the category of light and ultralight aircraft. Recently, other ultralight aircraft have been modified and sold in an STOL version. The Savannah ADV (see Fig. 3) produced by ICP was put on the market in 2005. These aircraft are usually characterized by a fuselage that is not very well streamlined and by a wing employing classic airfoil shape. For example, the Savannah ADV employs a NACA 5-digit airfoil and a very simple flap shape. Some STOL aircraft in this category are characterized by a fixed slot at the leading edge (see Fig. 4) penalizing parasite drag and flight speed in cruise conditions. The initial idea on which the EasyFly project was based was to design a STOL ultralight aircraft made of composite material with good drag characteristics and very low stalling speed. The wing high-lift system (flap and slat) was specifically designed to have low-drag characteristics in cruise conditions and a very high maximum lift coefficient in full-flap configuration; to achieve this, both leading-edge slat and slotted flap were designed to be retractable.

The general design of the aircraft was presented in previous papers [1–3]. The aerodynamic design of both the main airfoil and high-lift system, performed through aerodynamic numerical analysis and wind-tunnel tests, are illustrated in the present paper.

The high-lift system includes a retractable slotted flap and a retractable slat. Most of the reports about three-element high-lift airfoils reported in current literature [4–7] refer to applications at a high Reynolds number and to airfoil shapes commonly used for general transport transonic aircraft. This paper presents the research work undertaken on high-lift devices to be applied for low-speed light and general aviation aircraft. A Reynolds number of about 1×10^6 at landing speed usually characterizes these applications. For this reason, particular attention has been paid to this factor in both the numerical analysis and in experimental tests, and the optimization of gap and overlap has been performed both numerically and experimentally. The final results in terms of maximum achieved lift coefficient are particularly promising because they were obtained for a relatively low Reynolds number.

II. Airfoil Design

A new airfoil was designed at the DIAS. The aerodynamic requirements were a $C_{l\,\max}$ of no less than 1.6 at a Reynolds number 1.7×10^6, a $C_{d\,\min}$ less than 0.006, and $C_{\text{mc}/4}$ greater than -0.08 at a Reynolds number 4×10^6; a 13.5% chord referred thickness was chosen to obtain a good compromise among wing weight, low drag, and high lift. Requirements regarding transition were also taken into account. In general, a certain amount of laminar flow is well accepted to reduce drag in cruise condition; in the present design, however, high-lift requirements have to be considered, and this means that instead of large extent of laminar flow, a moderate laminar flow is preferable if a very gradual asset-related change in transition point can be achieved at the same time. In this way, it should be possible to avoid abrupt stall, often connected with laminar bubble and/or transition instabilities.

Received 26 January 2009; revision received 20 April 2009; accepted for publication 20 April 2009. Copyright © 2009 by the American Institute of Aeronautics and Astronautics, Inc. All rights reserved. Copies of this paper may be made for personal or internal use, on condition that the copier pay the $10.00 per-copy fee to the Copyright Clearance Center, Inc., 222 Rosewood Drive, Danvers, MA 01923; include the code 0021-8669/09 and $10.00 in correspondence with the CCC.

*Associate Professor, Department of Aerospace Engineering, Via Claudio 21; coiro@unina.it. Senior Member AIAA.

†Assistant Professor, Department of Aerospace Engineering, Via Claudio 21; fabrnico@unina.it. Senior Member AIAA.

‡Postdoctoral Aerodynamicist, Department of Aerospace Engineering, Via Claudio 21; francesco.grasso@unina.it. Associate Fellow AIAA.

Fig. 1 Perspective CAD view of EasyFly aircraft.

Fig. 2 CH701 aircraft.

Fig. 3 Savannah ADV aircraft.

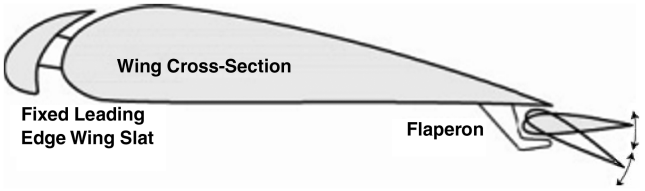

Fig. 4 CH701 wing section.

Another reason that a moderate extent of laminar flow was required was connected with the high-lift system. To ensure STOL performances, the high-lift system (Sec. III) also includes a slat; the junction between slat and main component can induce a premature transition, nullifying any large amount of laminar flow.

The adopted design methodology [8] included a preliminary airfoil selection to obtain a starting airfoil shape that was not too far from the design requirements. The design loop (see Fig. 5) included the evaluation of both airfoil aerodynamics and complete aircraft aerodynamics and performances. The airfoil's aerodynamic characteristics were calculated using XFOIL [9] and TBVOR [10–12] codes; aircraft performances were calculated using AEREO [13]

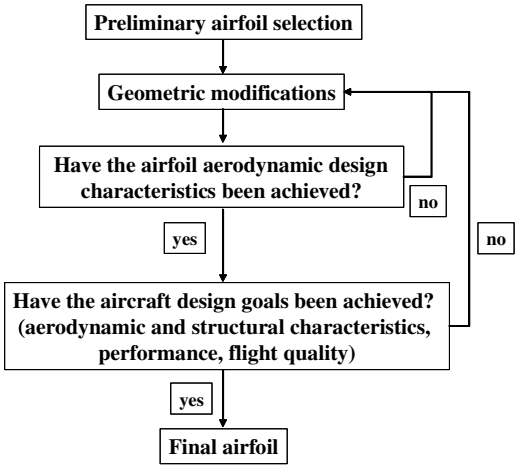

Fig. 5 Airfoil design loop.

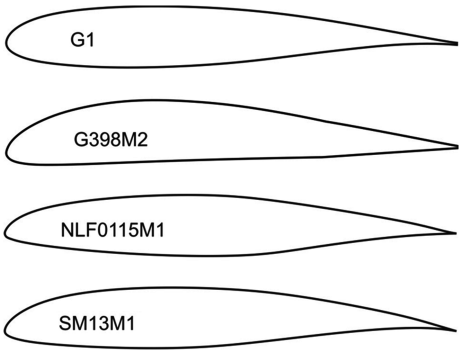

Fig. 6 Compared airfoil geometries.

numerical code. For all calculations, the Reynolds number was constant.

The GAW(1) airfoil was taken as a preliminary airfoil shape. Airfoil thickness was then reduced from 16 to 13.5% and the resulting airfoil was named GAW(1)M.

To modify the GAW(1)M geometry, standard geometric manipulation tools were used. During the first phase of this geometrical modification step, the shape of the leading edge (LE) and camber characteristics were mainly taken into account; transition location and laminar extent analysis were used as an a posteriori check. First, the maximum camber of the mean line was reduced and its position was moved forward to improve the $C_{\mathrm{mc}/4}$. The LE was slightly dropped to achieve high-lift performance; at the same time, its radius was increased to obtain good stall characteristics and to avoid abrupt stalling. In terms of transition behavior, the quite round LE shape and the maximum thickness location around the 37% of the chord guarantee a 40% laminar flow extension and a very stable trailing-edge (TE) turbulent separation. The resultant airfoil was named G1. The G1 airfoil was compared with several other modified airfoils, such as the NLF0115 (13.5% thickness reduced and renamed NLF0115M1), the SM13m1 (a modification of the SM701 airfoil), and the G398m2 (a modification of the Gottingen G398 airfoil) (see Fig. 6).

Table 1 compares the main aerodynamic characteristics (estimated through the use of the aforementioned aerodynamic codes [9–12]) of

Table 1 Airfoil aerodynamic characteristics (TBVOR)

Airfoil	$C_{l\max}$ $Re = 1.7 \times 10^6$	$C_{d\min}$ $Re = 4 \times 10^6$	$C_{\mathrm{mc}/4}$ $Re = 4 \times 10^6$
G1	1.67	0.00530	−0.0711
NLF0115	1.47	0.00418	−0.0521
G398m2	1.43	0.00531	−0.066
SM13m1	1.81	0.00496	−0.125

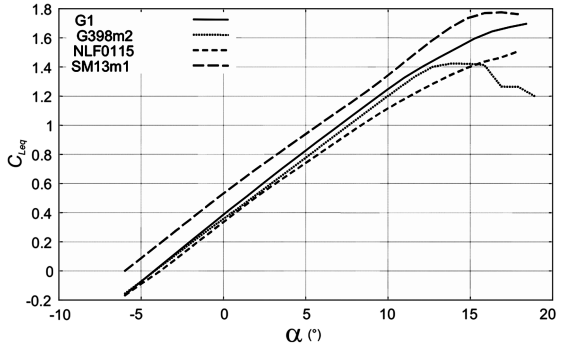

Fig. 7 Effect of airfoil on aircraft trimmed lift curve; AEREO calculations.

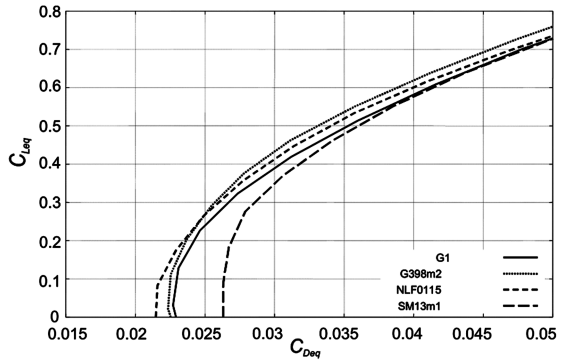

Fig. 8 Effect of airfoil on aircraft trimmed drag polar; AEREO calculations.

the aforementioned airfoils. The estimated two-dimensional airfoil aerodynamic was then used to evaluate [13] the aerodynamic characteristics of the complete aircraft. Figures 7 and 8 show the effect of airfoil shape on the aircraft trimmed lift-coefficient curve and on the aircraft trimmed polar. The main aircraft performances were estimated on the basis of predicted aircraft maximum lift and aircraft trimmed polar [13] and these are presented in Table 2.

Table 2 presents the estimated aircraft performance parameters, including maximum level speed, stalling speed (flap up and down), and maximum rate of climb RC_{max}. The last column of Table 2 shows the maximum tail load (at maximum flight speed) $Lh_{V\max}$ on the horizontal tail surface necessary to equilibrate the aircraft at maximum leveled speed. It is well known that high airfoil pitching moment (see Table 1) leads to high value of tail loading. The G1 airfoil can be considered as a good compromise between STOL performance and cruise performance, except for the associated tail load Lh, especially if compared with NLF0115M1 characteristics. This airfoil is well suited for low drag applications and it is very sensitive to transition location. From this point of view, the G1 airfoil is more robust, but its Lh characteristics have to be enhanced, also because high Lh means high structural tail weight and high trim drag. To improve this aspect and try to save the other G1 good characteristics, the airfoil TE was rotated 3 deg upward. The resultant airfoil was named G1F (see Fig. 9). An analysis extended to stall and

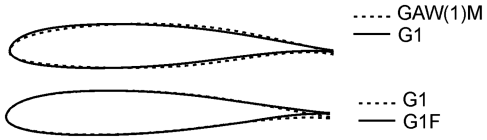

Fig. 9 Comparison between GAW(1)M and G1 and between G1 and G1F airfoil geometries.

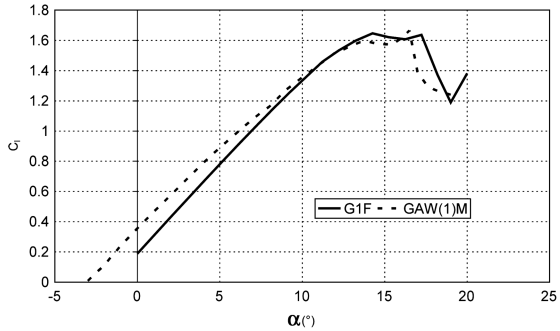

Fig. 10 Lift curve of GAW(1)M and G1F airfoils; TBVOR results ($Re = 2 \times 10^6$ constant).

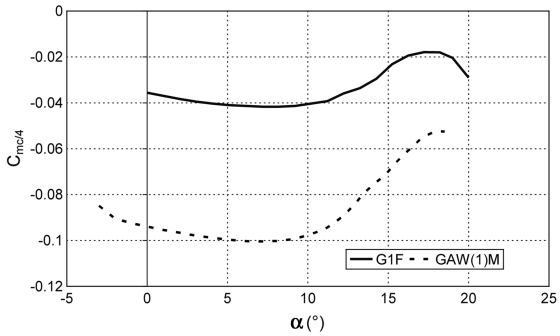

Fig. 11 Pitching moment curve of GAW(1)M and G1F airfoils; TBVOR results ($Re = 2 \times 10^6$ constant).

poststall conditions was performed to check the influence of geometry modification on maximum lift coefficient. The lift curve and moment coefficient are shown in Figs. 10 and 11; this analysis was performed considering transition placed at about 10% on both the upper and lower surfaces, to simulate the presence of slat. It can be seen that the maximum lift coefficient at $Re = 2 \times 10^6$ of the G1F airfoil is very close to that of the original GAW(1)M airfoil. A value close to 1.60 was estimated. Figure 11 shows that the G1F is characterized by a very low pitching moment coefficient (about −0.040) compared with that (−0.10) of the GAW(1)M airfoil. In terms of drag characteristics, the G1F airfoil has similar drag coefficient values (around 0.0060 at $Re = 4 \times 10^6$) to those of the GAW(1)M, showing some laminar flow extension on the upper and lower surfaces. Figure 12 shows the location for transition and separation point calculated by using TBVOR in free transition at $Re = 2 \times 10^6$; transition location moves very gradually and separation occurs just at high assets.

Table 2 Effect of airfoil shape on complete aircraft performances (AEREO)

			V_{sff}, km/h			
Airfoil	V_{max}, km/h	V_s, Km/h	Slat with single-slot flap	Slat with Fowler flap	RC_{max}, m/s	$Lh_{V\max}$, kg
G1	194.095	64.926	47.568	45.565	6.69	−159.63
NLF0115M1	194.529	69.457	49.266	47.051	6.85	42.77
G398m2	194.769	67.456	48.537	46.414	6.78	−104.77
SM13m1	191.508	62.172	46.453	44.581	6.63	−310.73

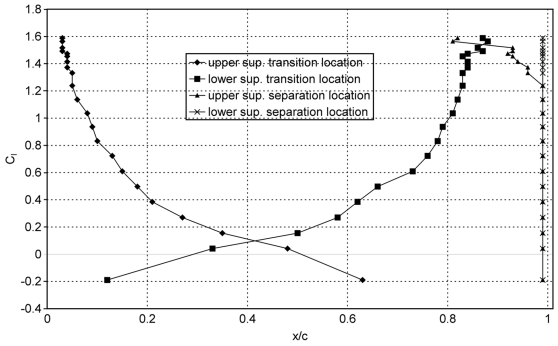

Fig. 12 Transition and separation location; TBVOR results ($Re = 2 \times 10^6$ constant).

III. High-Lift System Design

A. Preliminary Sizing Procedure and High-Lift Design Loop

A sizing procedure based on Roskam's semi-empirical methodology [14] was applied to obtain some preliminary indications about a two-dimensional high-lift system that could satisfy design specifications. Two solutions in particular were considered for the flap: single-slotted and Fowler. A flap chord extension of about 30% was considered to optimize flap effectiveness and to contain the increase of wing pitching moment; a chord extension of 15% for the slat was considered. Table 3 shows the results of this preliminary analysis.

It can be seen that, starting from a clean airfoil with $C_{l\max}$ of 1.60, a $C_{l\max}$ for the flapped configuration of 3.46 can be achieved with a slotted-flap slat configuration. Although it is possible to obtain a better value of $C_{l\max}$ by adopting the Fowler flap, the single-slot flap was chosen because the Fowler is heavier, more complex, and more expensive; it is thus not compatible with light and ultralight aircraft.

Figure 13 shows the high-lift design loop. Taking the semi-empirical results to be the aerodynamic requirements, and starting from a single-component airfoil, the slat and flap were separately designed. Subsequently, the complete high-lift configuration was developed and optimized through numerical computations [15–17]. Landing was prescribed as the condition for the design configuration, and all the analyses were performed at a constant Reynolds number of 1.3×10^6 by using MSES [18] code.

B. Single-Slot Flap Design

To obtain a value of C_l of not less than 3.4 at the angle of attack of 10 deg with a 40 deg flap deflection, different shapes were developed by working on the flap shape, slot shape, and lip extension. Figure 14 shows some of the configurations and Table 4 presents the results.

C. Slat Design

Similarly, to achieve a C_l of not less than 1.9 at a 15 deg angle of attack and starting from a single-component airfoil, different slat geometries were designed by modifying both slat and slot shapes. A 25 deg deflection angle and a slat chord of 15% with respect to the whole airfoil chord were established by the preliminary sizing process. Figure 15 shows some of the configurations and Table 5 presents the results. Starting from the $s2$ configuration, the $s4$ configuration was obtained by cutting the trailing-edge area to simplify the slat manufacturing.

D. Complete Configuration Modifications and Analysis

The three-component configuration was obtained by merging $fs6$ flap geometry and $s4$ slat geometry. The single-slotted flap rotates on

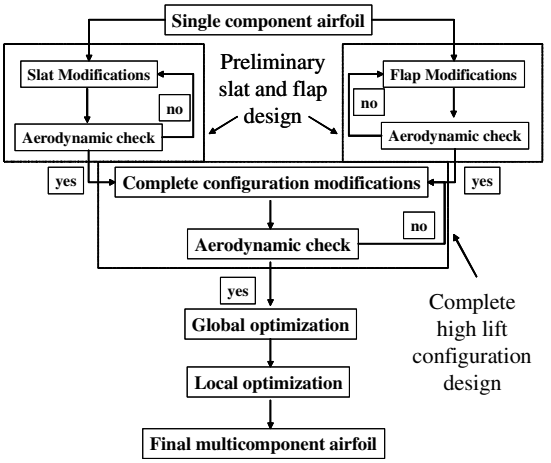

Fig. 13 High-lift design loop

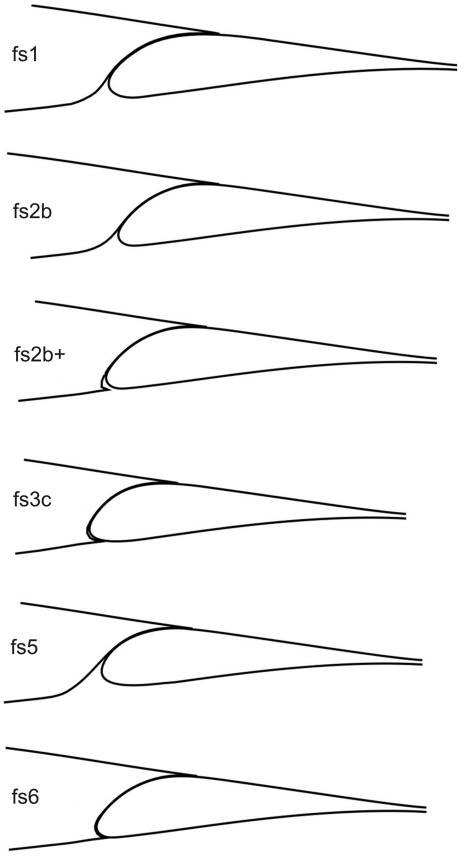

Fig. 14 Developed flap configurations.

Table 4 Maximum lift coefficient of the analyzed configurations (MSES) at $\alpha = 10$ deg

Configuration	$fs1$	$fs2b$	$fs2b+$	$fs3c$	$fs5$	$fs6$
C_l	3.41	3.34	3.38	3.25	3.18	3.46

Table 3 Airfoil maximum lift coefficient at different high-lift configurations

	Clean	Single-slot flap	Fowler flap	slat	Single slot with slat	Fowler with slat
Takeoff	1.6	2.23	2.28	2.07	2.65	2.70
Landing	1.6	3.03	3.45	2.07	3.46	3.87

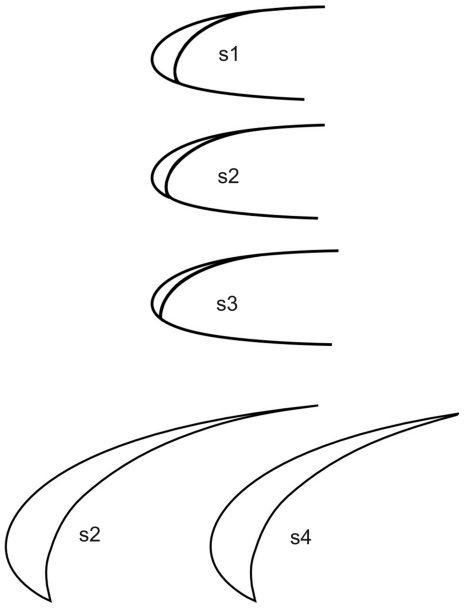

Fig. 15 Developed slat configurations.

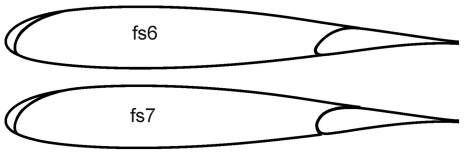

Fig. 16 G1F three components airfoil before and after modification.

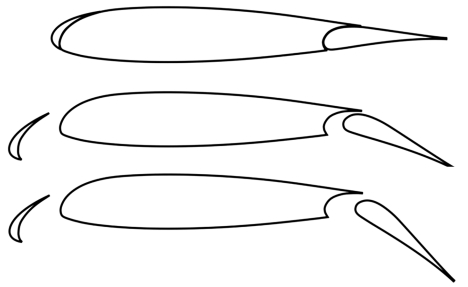

Fig. 17 G1F three components in cruise, takeoff, and landing configurations.

a hinge, and to reduce the forces acting upon the hinge point, the flap leading edge was modified. Figure 16 shows the new shape, named $fs7$, and the old one. Figure 17 shows the 3-component airfoil in cruise, takeoff (flap: 20 deg; slat: 25 deg), and landing (flap: 40 deg; slat: 20 deg) configurations. Figure 18 shows the results of the MSES analysis for the landing configuration. Figure 19 shows the grid used for the MSES analysis at an angle of attack of 18 deg.

E. Numerical Optimization

To enhance maximum lift performance parameters of the multicomponent airfoil in the landing configuration, a numerical optimization was carried out by varying slat and flap position in terms of gap and overlap. This optimization process was performed moving the flap and slat separately using a preestablished sets of positions.

1. Flap Position Optimization

Various configurations with different flap positions while keeping the slat fixed were analyzed with MSES, assuming the gap to be the minimum distance between the elements and the overlap to be the horizontal distance between the main component TE and flap LE (see Fig. 20).

For the overlap, an upper bound equal to 0.03 was chosen to avoid an excessive overlap with the consequent difficulties to properly address the flow in the slot; at the same time, a nonnegative lower bound was used to avoid configurations without a slot. Regarding the gap, it has been preferred to avoid very low gap values because of the MSES code tendency to overestimate lift performances in these cases; a maximum gap equal to 0.02 was chosen. Table 6 shows the explored geometries (in terms of gap and overlap) and Table 7 presents the calculated C_l of all configurations calculated by MSES at a 18.5 deg angle of attack.

The configurations $f3$, $f10$, $f11$, and $f14$ were selected by examining the results and the lift curves. Figure 21 shows the pressure coefficient distribution on the main component and flap of these geometries. Even if the $f3$ configuration should be the best configuration, the $f10$, $f11$, and $f14$ configurations were preferred because of the aforementioned tendency of the MSES code. The $f11$ configuration performs slightly better because of the smaller flap

Table 5 Maximum lift coefficient of the analyzed configurations (MSES) at $\alpha = 15$ deg

Configuration	$s1$	$s2$	$s3$	$s4$
C_l	1.92	1.95	1.93	1.95

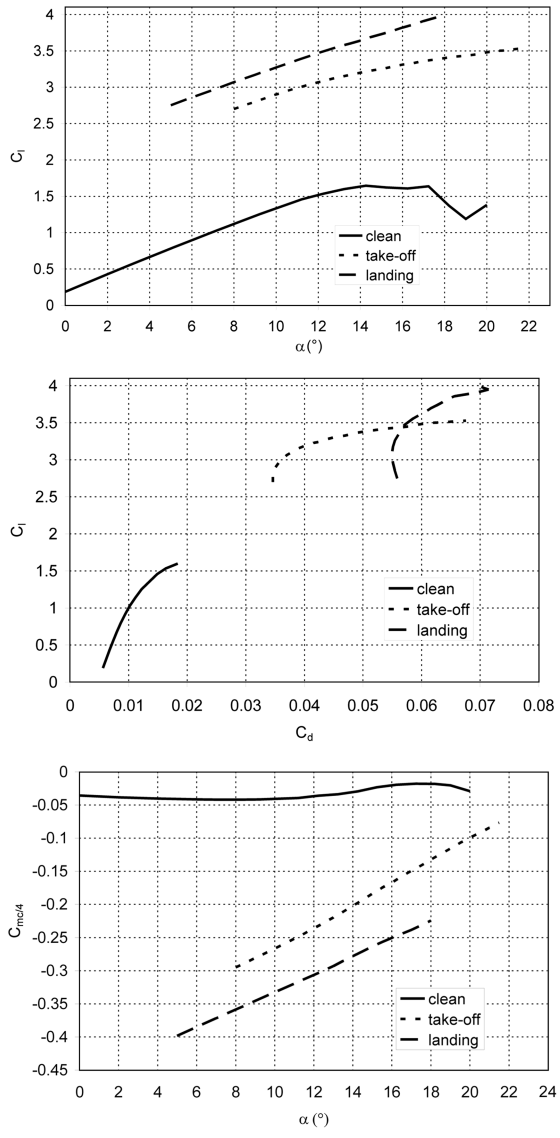

Fig. 18 Multi-element airfoil's geometry and aerodynamic characteristics ($Re = 1.3 \times 10^6$ constant).

overlap, but the $f14$ configuration was preferred because of hinge location considerations. For the $f14$ configuration, the hinge point is closer to the main element (compared with the $f11$); this means that the hinge moment is less intense and, consequently, the hinge support structure can be lighter and cheaper than that for the $f11$ configuration. Both weight and cost are very important for an ultralight aircraft. Figure 22 shows the hinge point locations for $f11$ and $f14$ configurations; the $f14$ support to the main component is the 20% shorter than the $f11$ support.

2. Slat Position Optimization

Different slat positions were examined, this time keeping the flap fixed, assuming that the gap is the minimum distance between elements and the overlap is the vertical distance between slat TE and main component LE (see Fig. 23).

Table 8 shows the explored geometries (again in terms of slat gap and overlap) and their C_l at an angle of attack of 18.5 deg (Table 9). Also for the slat, gap and overlap bounds were prescribed by taking

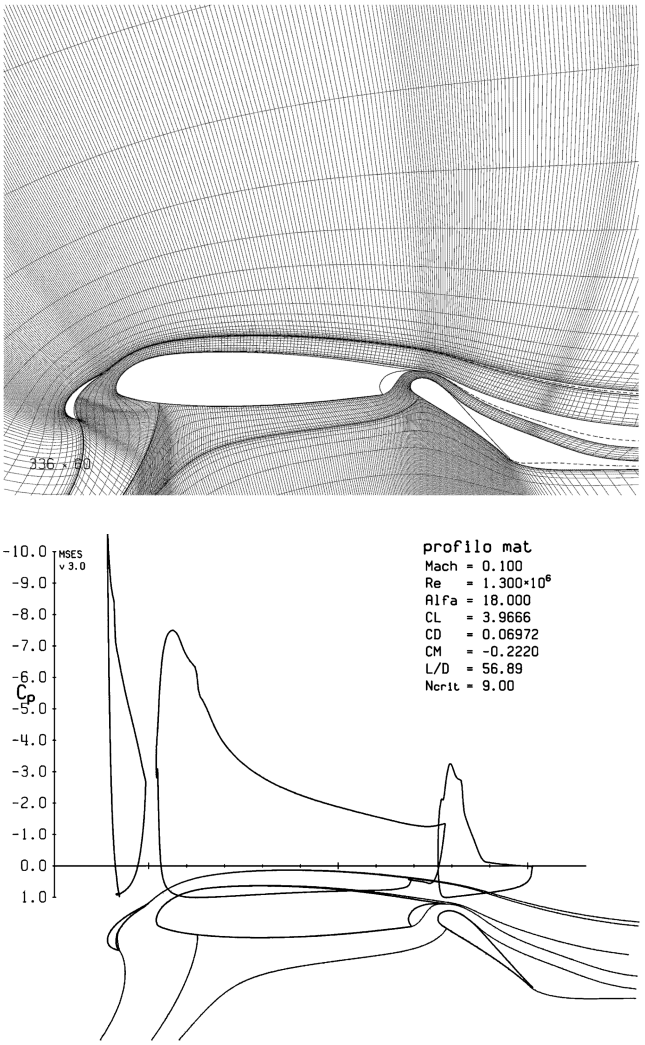

Fig. 19 Grid computed by MSES at angle of attack of 18 deg and pressure coefficient distribution at the same angle of attack.

Table 6 Geometrical characteristics of the analyzed configurations

	Overlap, %c			
Gap, %c	3	1.9	1	0
1.7	$f1$	$f2$	$f3$	$f4$
1.8	$f5$	$f6$	$f7$	$f8$
1.88	$f9$	$f10$	$f11$	$f12$
2	$f13$	$f14$	$f15$	$f16$

Table 7 Lift coefficient at $\alpha = 18.5$ deg (MSES)

	Overlap, %c			
Gap, %c	3	1.9	1	0
1.7	1.32	4.01	4.03	3.97
1.8	3.83	3.95	3.99	3.93
1.88	3.87	4	4.02	3.87
2	3.92	4	3.98	3.88

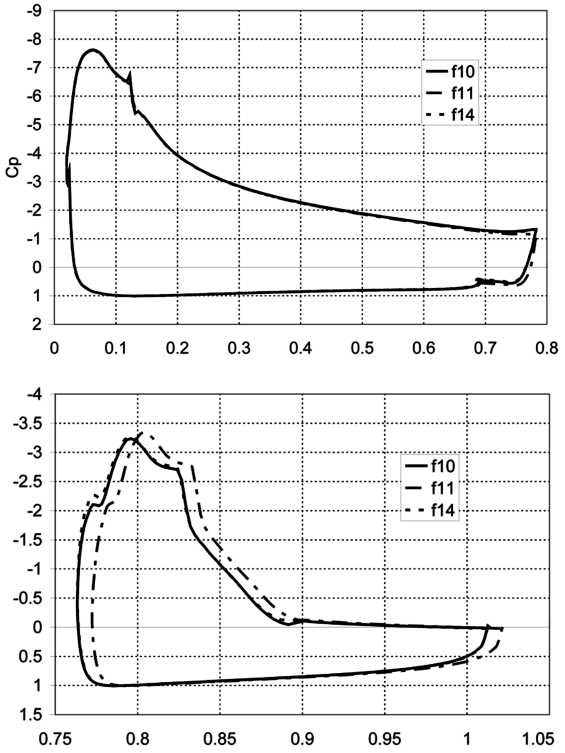

Fig. 21 Pressure coefficient distribution over main component and flap of G1F airfoil; MSES results at 18.5 deg.

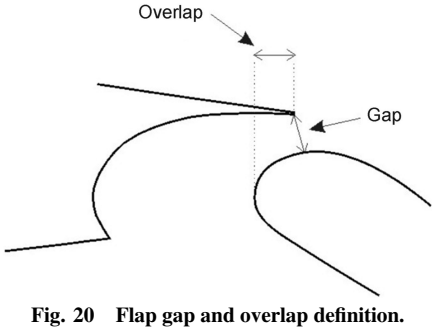

Fig. 20 Flap gap and overlap definition.

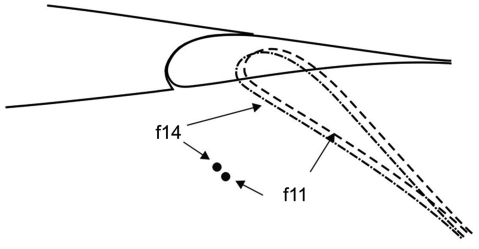

Fig. 22 Hinge point location.

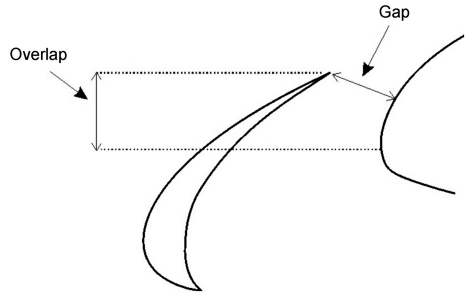

Fig. 23 Slat gap and overlap definition.

into account feasibility and expected performance considerations In this case, the choice is easier: the $s15$ configuration was selected.

IV. Wind-Tunnel Tests

After the in-depth numerical analysis, extensive tests, including both pressure measurements and flow visualizations, were performed on a 2-D model of the three-component G1F airfoil to obtain aerodynamic characteristics experimentally to validate the numerical results. This model was made using the flap and a main component made of aluminum using computer numerical control manufacturing. A very stiff carbon-fiber slat was built to avoid slat deformation at the center of the model, in which pressure taps were placed. The model has a chord of about 55 cm with the flap and the slat retracted, and Fig. 24 shows it installed in the test section along with a wake-rake with 80 pressure points employed to measure airfoil drag. A total of 18 pressure taps were installed on the slat, 65 on the main component, and 33 on the flap, giving a total number of about 116 pressure taps installed.

All tests were performed in the DIAS main wind tunnel (see Table 10 and Fig. 25); this facility is a closed-circuit wind tunnel with a closed test section measuring 2.0×1.4 m with a measured turbulence level equal to 0.1%. Tests also focused on optimizing the relative position of elements.

Two 64-channel ZOC Scanivalve pressure transducers [with full scale (FS) of 2500 Pa and accuracy 0.05–0.10%FS, and so about 1.25–2.50 Pa] were used for the pressure measurements. A very accurate ($\sim$1 Pa accuracy) automatic reading liquid multimanometer was used to measure wake-rake total and static pressures. During tests, the corrections due to model blockage, wake blockage, and solid-wall presence were taken into account, as reported by Rae and Pope [19]. An external suction system was used to minimize the tunnel sidewall effects (see Fig. 26). Drag was obtained by integration of pressures measured with the wake-rake. An estimation of experimental error based on instrumentation accuracy and model accuracy was determined, and it is equal to 2% of the pressure measurement.

Table 8 Scheme of the analyzed configurations

	Overlap, %c			
Gap, %c	8	6	4	1
3	$s1$	$s2$	$s3$	$s4$
3.5	$s5$	$s6$	$s7$	$s8$
3.77	$s13$	$s14$	$s15$	$s16$
4	$s9$	$s10$	$s11$	$s12$

Table 9 Lift coefficient at $\alpha = 18.5$ deg (MSES)

	Overlap, %c			
Gap, %c	8	6	4	1
3	3.71	3.91	3.86	3.8
3.5	1.09	3.91	3.94	3.88
3.77	3.77	3.91	3.96	3.76
4	3.78	3.91	3.9	3.76

Table 10 Wind-tunnel main characteristics

Test section dimensions	2.0×1.4 m
Maximum speed	150 km/h
Turbulence level	0.1%

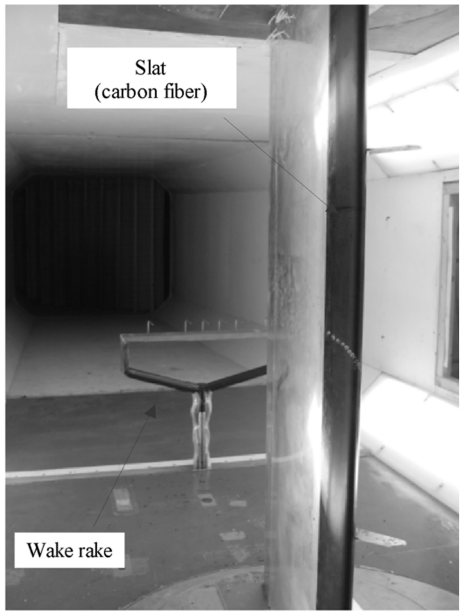

Fig. 24 Three-component G1F airfoil model.

A. Cruise Configuration

The first tests were conducted on the cruise configuration (flap and slat retracted); the test Reynolds number was 1.3×10^6, based on the model chord ($c = 0.55$ m). Figure 27 shows some flow visualizations made with fluorescent oil on the airfoil upper surface at angles of attack of 0 and 8 deg. At low angles of attack it can be observed that the geometrical discontinuity on the airfoil upper surface due to the slat trailing edge moves the transition toward the leading edge. This discontinuity causes an absence of laminar flow on the main component upper surface, as already outlined in this paper. This fact will cause higher airfoil drag than expected by numerical calculations with free transition. When the angle of attack is close to 8 deg, a laminar bubble appears on the slat upper surface, which moves the transition ahead of discontinuity. Increasing the angle of attack, the bubble moves forward at 5% of the chord, as Fig. 27 shows. The same tests were repeated setting a transition strip at 5% of the chord.

Figure 28 compares the numerical and the experimental results in terms of airfoil pressure coefficient distribution. In general, the numerical and experimental data agree well, except for the local difference on the upper surface of the airfoil due to the geometrical discontinuity between the slat and main component of the model.

Figures 29 and 30 show the comparisons between numerical and experimental analyses in terms of lift and drag coefficients. Once again, there is a good agreement between numerical and experimental results regarding the lift, whereas the slight disagreement shown for the drag polar curve is probably caused by an underestimation of numerical values and an excess of experimental drag arising from the aforementioned discontinuity not present in the geometry numerically analyzed.

B. Landing Configuration

The landing configuration was also tested extensively. The chosen preliminary landing configurations were obtained by considering the results of the previous numerical analysis. Thereafter, an experimental optimization of the configuration was carried out that

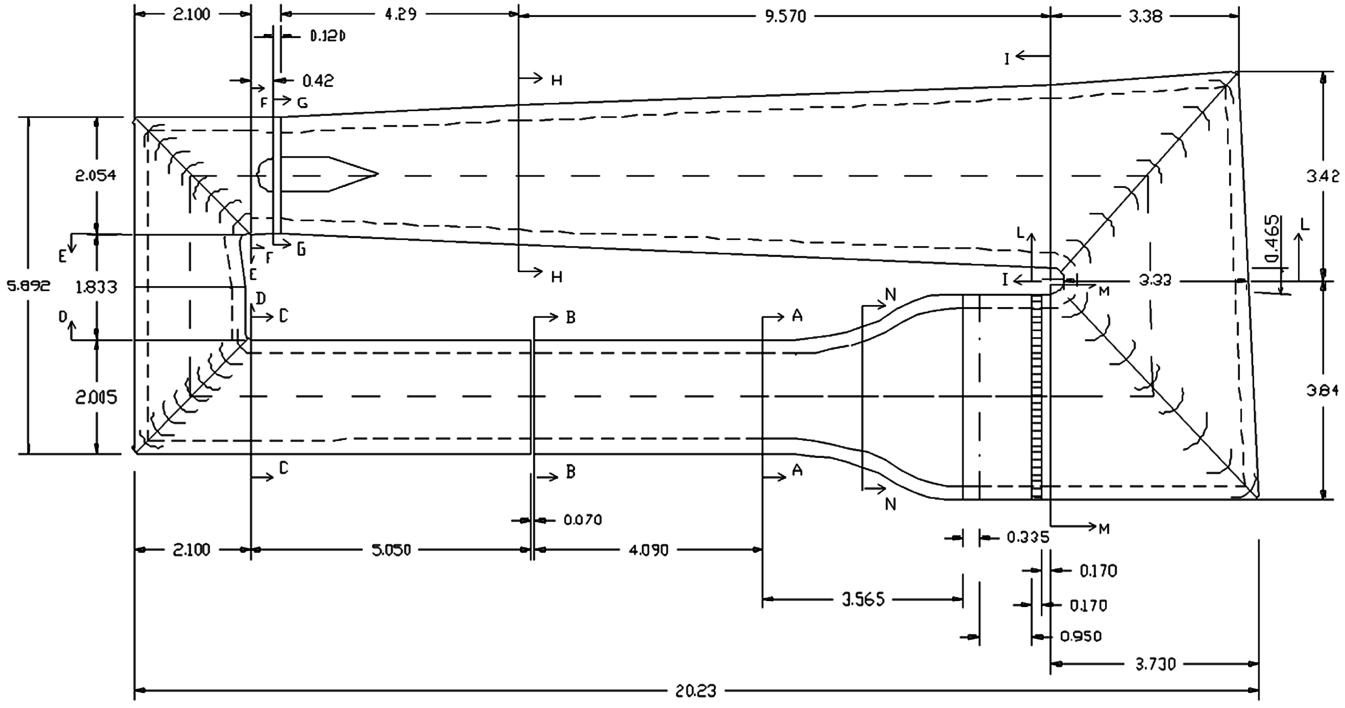

Fig. 25 Scheme of the wind tunnel at the DIAS.

acted separately on slat and flap position; the same definitions of gap and overlap used for the numerical analysis were also applied here.

Different slat configurations were analyzed at an angle of attack of 15 deg, assuming the same convention used during the numerical optimization. From Table 11 it can be seen that maximum lift coefficient for landing configuration is dependent on the slat gap and overlap. Table 11 shows that high values of the slat gap (5–6%, configurations $s2$ and $s3$) are characterized by a reduction of maximum achievable lift coefficient compared with the $s1$ configuration (gap of about 3%). An overlap of about 4% was found to be the best. Very small slat gap and overlap values (configuration $s4$) led to a partially chocked slat channel with a noticeable reduction of maximum lift coefficient. Finally, a slat position close to $s1$ (gap of 3% and overlap of about 4% of airfoil chord) was chosen and kept unchanged for the next set of experiments on flap position optimization.

In the same way, different flap configurations were considered with a deflection of 39 deg (see Table 12), assuming the same convention introduced during the numerical optimization. As can be seen from Table 12, the gap of the tested configuration was set at about 1.3% of airfoil chord. Preliminary tests (see also $p1$ in Table 12) showed that a smaller flap gap value (see, for example, configuration $p1$ with gap value of 1.18%) led to a partially chocked channel (with the flap not working properly) and a lower maximum lift coefficient. The different configurations reported in Table 12 have overlap values ranging from 2 to about 4% of the chord. It is well established that very low overlap values lead to an inefficient slot with increased flow separation on the flap upper surface. Figure 31 shows the comparison between the different lift-coefficient curves measured by wind-tunnel tests performed on each configuration. As can be seen in

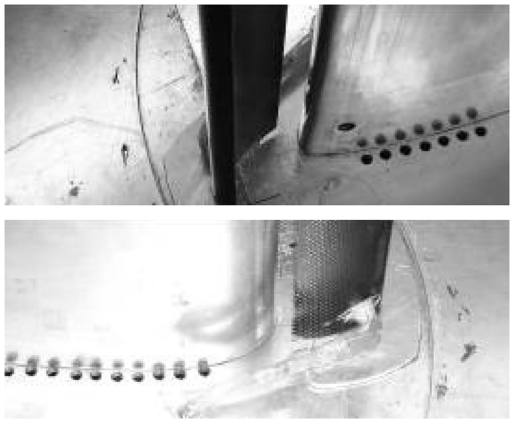

Fig. 26 Suction system holes.

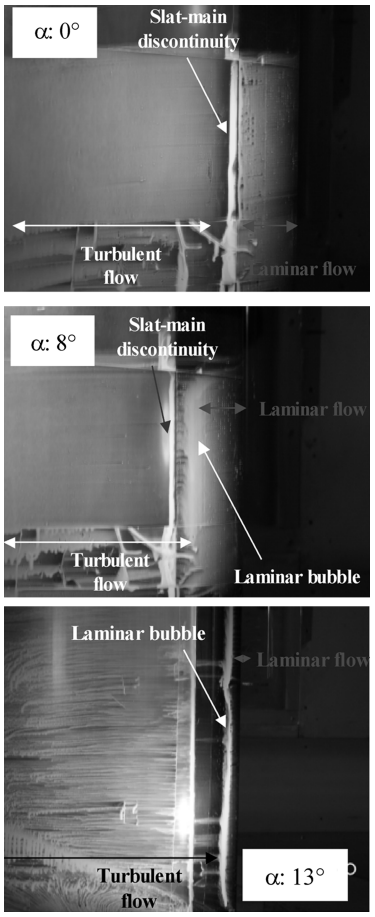

Fig. 27 Flow visualization tests on airfoil upper surface.

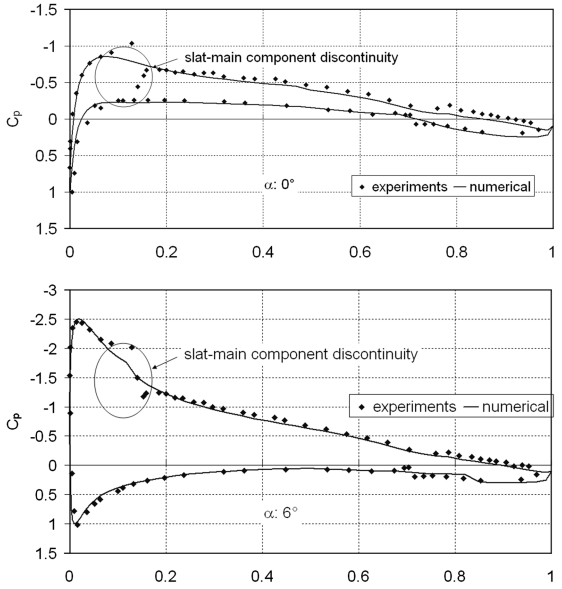

Fig. 28 Pressure coefficient measurements on G1F airfoil, numerical-experimental comparisons; numerical results obtained by using TBVOR.

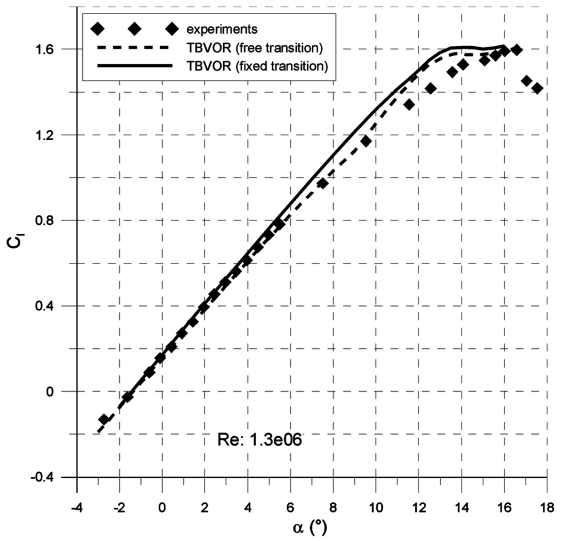

Fig. 29 Lift curve, numerical-experimental comparisons; numerical results obtained by using TBVOR.

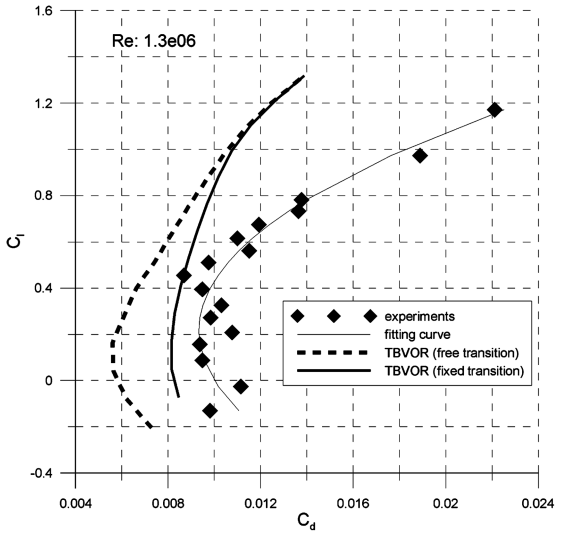

Fig. 30 Drag curve, numerical-experimental comparisons; numerical results obtained by using TBVOR.

Table 11 Slat position experimental optimization; $Re = 1.3 \times 10^6$, flap deflection is 39 deg, and slat deflection is 0 deg.

Configuration	Gap, %c	Overlap, %c	α, deg	C_l
$s1$	3.37	4.12	15.37	3.7
$s2$	5.1	3.9	15.5	3.3
$s3$	6.1	4.44	15.46	3.5
$s4$	2.22	2.56	15.36	3.22

Table 12 Flap position experimental optimization; $Re = 1.3 \times 10^6$, flap deflection is 39 deg, and slat deflection is 0 deg.

Configuration	Gap, %c	Overlap, %c
$p1$	1.18	2.3
$p2$	1.35	3.4
$p3$	1.35	3.2
$p4$	1.35	1.96
$p5$	1.35	3.73

Fig. 31, an overlap of about 4% with gap fixed at 1.35% (configuration $p5$) was found to be optimal. The maximum lift coefficient measured for the final landing configuration at an angle of attack of about 24 deg is about 4.0. This can be considered as a very high value for maximum lift coefficient and thus a highly satisfactory outcome of the numerical and experimental optimization process.

Figure 32 shows the pressure coefficient distribution measured on the 3-component airfoil in the landing configuration at different angles of attack. Lift-coefficient contributions of each element are also reported in the same figure. Note that the increase in lift

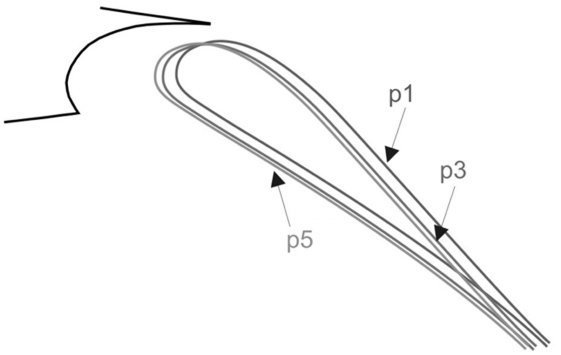

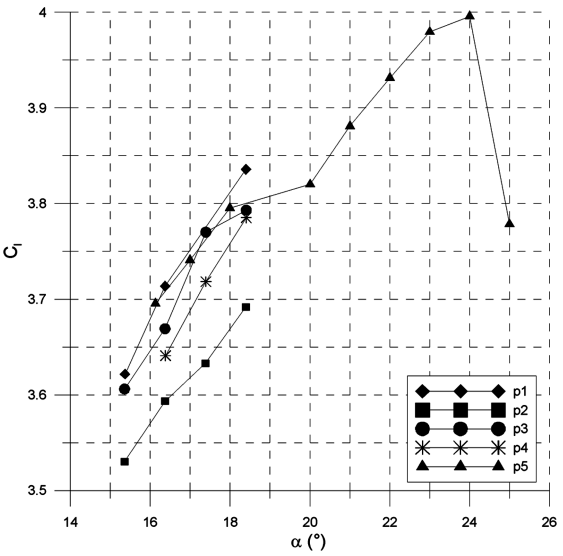

Fig. 31 lift-coefficient curve of experimentally optimized flap configurations ($Re = 1.3 \times 10^6$).

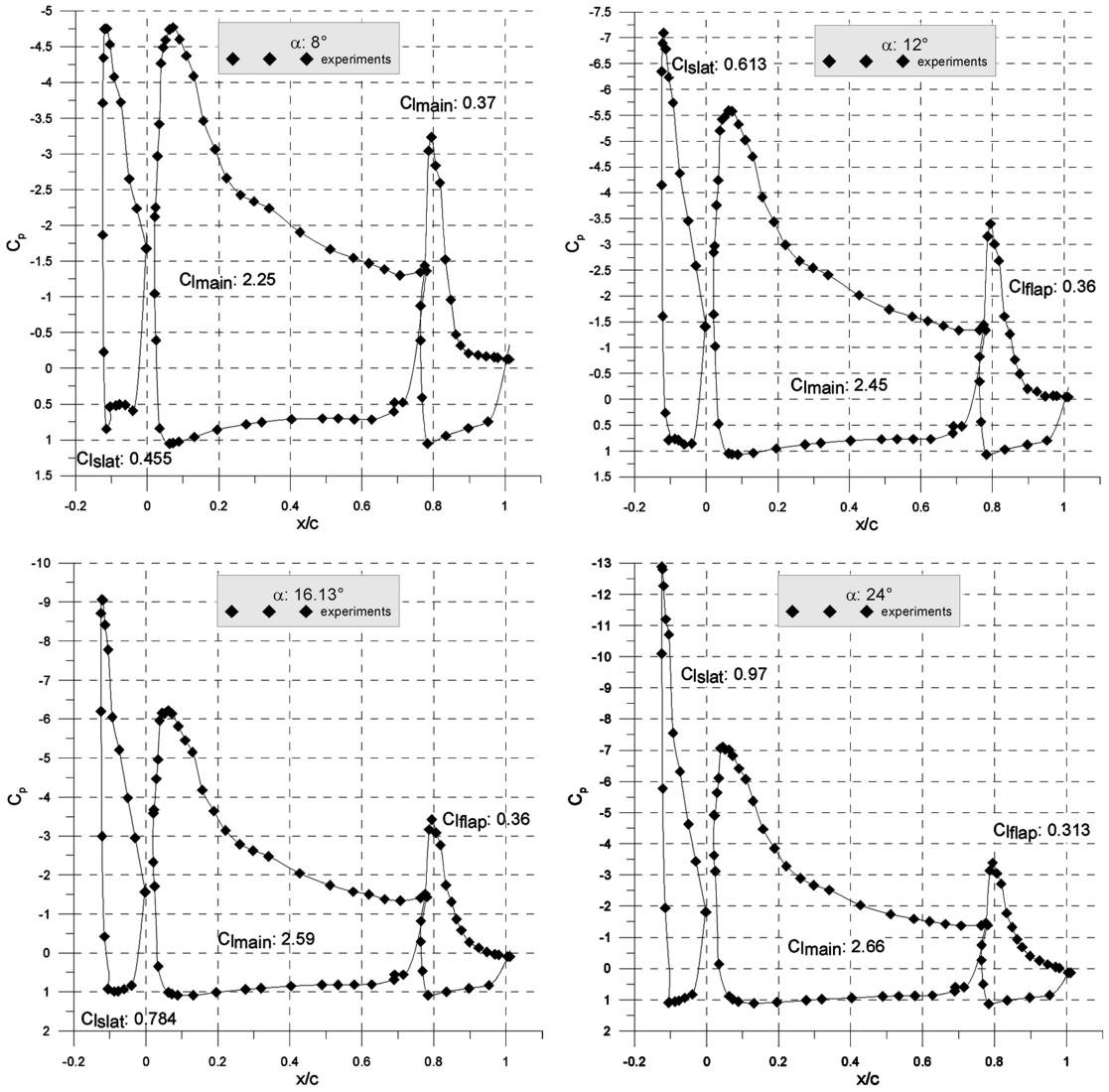

Fig. 32 Experimental pressure coefficient distribution of landing configuration at different angles of attack; $Re = 1.3 \times 10^6$, flap deflection is 39 deg, and slat deflection is 0 deg.

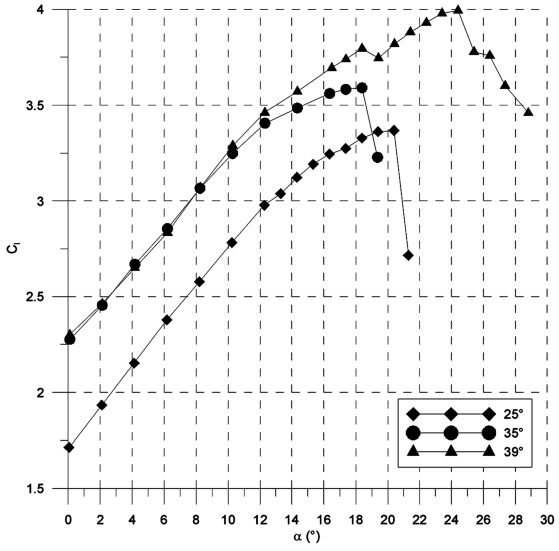

Fig. 33 Experimental lift-coefficient curve of the landing configuration; effect of the flap deflection angle. $Re = 1.3 \times 10^6$, flap deflection is 39 deg, and slat deflection is 0 deg.

coefficient from an angle of attack of 12 to 24 deg is mainly due to the marked increase in lift on the slat component. From 12 to 24 deg, the main component lift coefficient increases by about 10%, whereas the lift coefficient on the slat increases from 0.61 up to about 1.0 (i.e., by about 65%).

Figure 33 shows the lift-coefficient curve of the optimal landing configuration; the effect of different flap deflection angles is also shown in the same figure. A maximum global lift coefficient is around 4, achieved at an angle of attack of 24 deg.

Tests on the landing configuration with fixed transition on the slat and on the main component were also performed to test the effect of dirt and roughness on the airfoil surface. A transition strip was applied to the slat leading edge and to the main leading edge (about

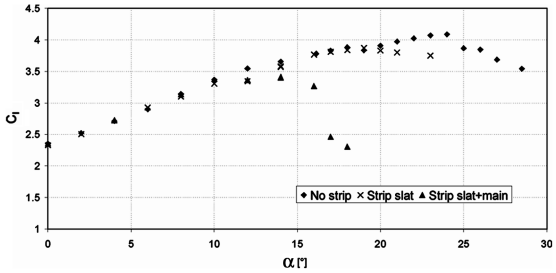

Fig. 34 Experimental lift curve with fixed transition effects; $Re = 1.3 \times 10^6$, flap deflection is 39 deg, and slat deflection is 0 deg.

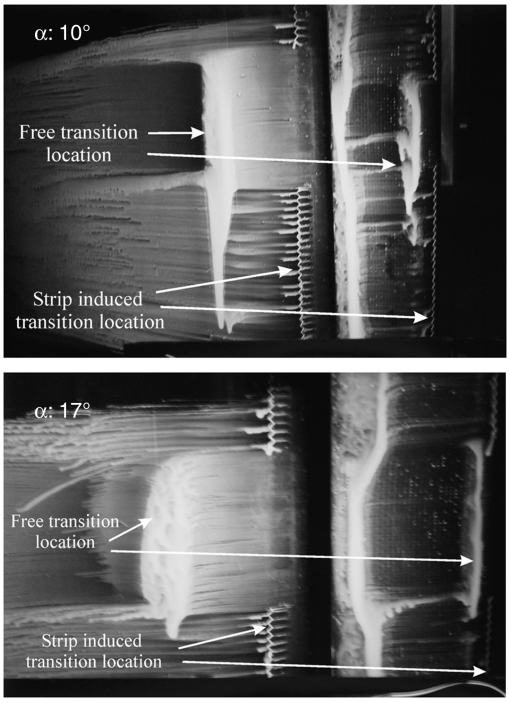

Fig. 35 Flow visualization tests on landing configuration upper surface (flow from right to left).

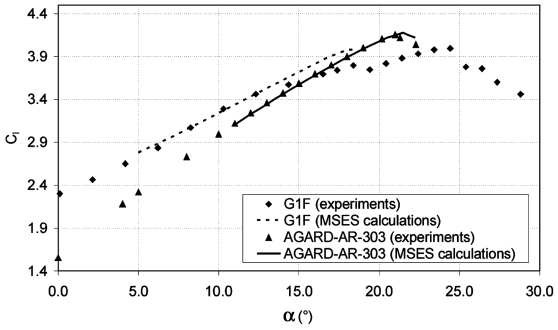

Fig. 36 Numerical-experimental comparison between G1F airfoil and AGARD AR-303 [6] airfoil.

5% of the main component on its upper surface). Figure 34 reports the results in terms of lift curve, and Fig. 35 shows pictures of the flow visualization tests.

At the end of numerical and experimental analysis, a comparison in terms of lift-coefficient curves was made between the final G1F three-element airfoil and the airfoil [6]. This was done because of the scarcity of literature about multi-element airfoils at a low Reynolds number, as highlighted in the Introduction. Figure 36 shows the experimental and numerical lift curves of the G1F 3-element airfoil at $Re = 1.3 \times 10^6$ compared with the experimental and numerical results of the AGARD AR-303 [6] test-case airfoil at $Re = 3.5 \times 10^6$. All numerical calculations were performed using the MSES code. Note that the airfoil presented in the AGARD [6] case is a three-component airfoil with a Fowler flap but with a lower flap deflection (about 20 deg.) than the G1F airfoil. The G1F airfoil shows a similar maximum lift coefficient despite the lower Reynolds number, due mainly to higher flap deflection. The experimental results show that a $C_{l\max}$ of about 4 is possible at a low Reynolds number (about 1×10^6) with a three-component airfoil and with adequate flap deflection.

V. Conclusions

Starting from the GAW(1) airfoil, the G1F airfoil was designed, numerically analyzed, and experimentally tested. This new airfoil is well suited to STOL applications, as it has good stall characteristics and high $C_{l\max}$ value. At the same time, the pitching moment coefficient $C_{\mathrm{mc}/4}$ is low (−0.040), leading to small tail loads and small trim drag for the aircraft. Experimental tests confirmed all the numerical results. The airfoil maximum lift coefficient in cruise configuration (slat and flap retracted) was found to be around 1.60 (both numerically and experimentally) at a Reynolds number of 1.3×10^6. A detailed numerical aerodynamic analysis of the 3-component landing configuration with flap and slat deflected was performed using the MSES code. Many different configurations were considered and these were obtained by modifying flap and slat positions (different gap and overlap values for both components). Calculations showed that a maximum multicomponent airfoil lift coefficient of about 4.0 could be achieved at high angles of attack at $Re = 1.3 \times 10^6$. The wind-tunnel tests were then performed on the landing configurations for the 3-component airfoils. An experimental optimization of flap and slat position, changing gap and overlap, was carried out for both components. More than 30 different configurations were tested using a wide range of angles of attack. In this paper, only the results relating to the more significant configurations have been presented. After flap and slat optimization, the final landing configuration shows a maximum lift coefficient close to 4.0. This can be regarded as a highly satisfactory result, considering the low value of Reynolds number. As a consequence of this, the present work can be considered as a good point of reference for the design of multi-element airfoils. The maximum lift coefficient achieved in the landing configuration provides good opportunities for the airfoil to be employed on STOL light aircraft. In Appendices A and B, the coordinates of the single-component airfoil (Table A1) and multicomponent airfoil (Tables B1–B3) are indicated.

Appendix A: G1F Single-Component Airfoil Coordinates

Table A1 G1F single-component airfoil coordinates

x/c	y/c
0.999774	0.000573
0.987277	0.001332
0.965208	0.003687
0.938837	0.007044
0.908922	0.011121
0.876884	0.015597
0.843993	0.020248
0.810867	0.025034
0.777551	0.029945
0.744315	0.034861
0.711392	0.03988
0.678507	0.045019
0.646121	0.049955
0.614228	0.054493
0.58259	0.058597
0.551039	0.062276
0.519501	0.065528
0.487928	0.068361
0.456311	0.070787
0.424672	0.072804
0.393058	0.074406
0.361508	0.075595
0.330106	0.076344
0.298939	0.076631
0.26814	0.076429
0.237852	0.075693
0.208385	0.074395
0.18007	0.072458
0.153266	0.069843
0.128439	0.066581
0.106154	0.062814
0.086864	0.058713
0.07059	0.05438
0.057021	0.049945

(continued)

Table A1 G1F single-component airfoil coordinates (Continued)

x/c	y/c
0.045766	0.04551
0.036424	0.041135
0.028646	0.036839
0.022154	0.032622
0.01673	0.028476
0.012215	0.024392
0.008498	0.020356
0.005496	0.016365
0.003166	0.012414
0.001483	0.008514
0.000435	0.00469
0.000011	0.000985
0.000193	−0.00266
0.001045	−0.00638
0.002627	−0.01011
0.004961	−0.01374
0.008045	−0.01724
0.011857	−0.02061
0.016463	−0.02383
0.021973	−0.0269
0.028502	−0.02991
0.036272	−0.03292
0.045608	−0.03597
0.056956	−0.03906
0.070887	−0.04219
0.088018	−0.04532
0.108733	−0.04839
0.132845	−0.05123
0.159747	−0.05364
0.188523	−0.0556
0.218418	−0.05702
0.249008	−0.05791
0.280082	−0.05831
0.311502	−0.05825
0.343152	−0.05777
0.374955	−0.05689
0.406818	−0.05564
0.43868	−0.054
0.470531	−0.05198
0.502413	−0.04957
0.534393	−0.04676
0.566579	−0.0436
0.599001	−0.04013
0.631477	−0.03646
0.66345	−0.03265
0.695651	−0.02828
0.728579	−0.02375
0.761529	−0.01924
0.794011	−0.01497
0.825842	−0.01098
0.856565	−0.00752
0.886232	−0.00476
0.914713	−0.00277
0.941555	−0.00161
0.966058	−0.00126
0.987538	−0.00167
1	−0.00242

Appendix B: G1F Three-Component Airfoil Coordinates (Landing Configuration)

Table B1 G1F slat coordinates

x/c	y/c
−0.00745	0.024986
−0.03215	0.012802
−0.05201	0.001377
−0.06747	−0.00905
−0.0793	−0.01843
−0.08832	−0.02689

(continued)

Table B1 G1F slat coordinates (Continued)

x/c	y/c
−0.09517	−0.03458
−0.10032	−0.04166
−0.10408	−0.04823
−0.10666	−0.05437
−0.10817	−0.06013
−0.10868	−0.0655
−0.10823	−0.07043
−0.10687	−0.07493
−0.10442	−0.07923
−0.10081	−0.08317
−0.09604	−0.08657
−0.09013	−0.0894
−0.08488	−0.09118
−0.08111	−0.09193
−0.07722	−0.09261
−0.07722	−0.09261
−0.08196	−0.08722
−0.08451	−0.08152
−0.08563	−0.07662
−0.08606	−0.07325
−0.08611	−0.06977
−0.0858	−0.06357
−0.08457	−0.05479
−0.08208	−0.04636
−0.07774	−0.03771
−0.07096	−0.02787
−0.06214	−0.01718
−0.05134	−0.00642
−0.03991	0.003069
−0.02661	0.012564
−0.00745	0.024986

Table B2 G1F main component coordinates

x/c	y/c
0.782345	0.030726
0.756731	0.03429
0.712575	0.040599
0.662578	0.047984
0.619642	0.054157
0.576587	0.059767
0.533788	0.06458
0.491009	0.068613
0.448176	0.071892
0.405353	0.074421
0.362698	0.076189
0.320474	0.077162
0.279097	0.077302
0.239344	0.076581
0.202501	0.075004
0.170152	0.072716
0.14309	0.069546
0.120313	0.065189
0.100994	0.059987
0.084753	0.054287
0.071232	0.048187
0.059984	0.041817
0.050648	0.035385
0.042954	0.029009
0.036678	0.022742
0.031657	0.016602
0.027712	0.010637
0.024705	0.004881
0.022422	−0.0006
0.0209	−0.00582
0.020041	−0.01088
0.020093	−0.01496
0.020718	−0.01923
0.021961	−0.02318
0.024022	−0.02657
0.028384	−0.02969

(continued)

Table B2 G1F main component coordinates (Continued)

x/c	y/c
0.03652	−0.03306
0.044531	−0.03567
0.05059	−0.03753
0.056599	−0.03916
0.066011	−0.04149
0.078444	−0.04427
0.094849	−0.0471
0.115842	−0.04999
0.142553	−0.05286
0.175106	−0.05548
0.212189	−0.0575
0.252088	−0.05872
0.293629	−0.05908
0.336144	−0.05865
0.3792	−0.05749
0.422475	−0.05562
0.465826	−0.05305
0.509309	−0.04976
0.553236	−0.04575
0.598001	−0.0411
0.643607	−0.03604
0.681976	−0.03138
0.693531	−0.02992
0.693531	−0.02992
0.689546	−0.0234
0.686076	−0.01466
0.686222	−0.00504
0.68893	0.001766
0.695551	0.01123
0.707462	0.020312
0.719487	0.025139
0.73218	0.028449
0.749045	0.030045
0.767119	0.030381
0.782378	0.029765

Table B3 Slotted flap coordinates

x/c	y/c
1.014122	−0.19102
1.000803	−0.17813
0.982767	−0.15907
0.961386	−0.13572
0.938427	−0.11028
0.914801	−0.08402
0.891316	−0.058
0.870098	−0.03491
0.851931	−0.01771
0.835627	−0.00496
0.821987	0.003515
0.810538	0.008601
0.800755	0.011187
0.79233	0.011887
0.785094	0.011107
0.778979	0.00932
0.773864	0.007152
0.769851	0.004468
0.766876	0.001334
0.76475	−0.00236
0.763516	−0.00667
0.763255	−0.0114
0.764422	−0.0163
0.767543	−0.02106
0.772716	−0.02582
0.780787	−0.03136
0.794076	−0.03985
0.815929	−0.05326
0.844692	−0.07083
0.875018	−0.08997
0.904873	−0.10962
0.933738	−0.12969
0.960608	−0.14961
0.984238	−0.16846
1.002829	−0.1845
1.012363	−0.19347

References

[1] Coiro, D. P., Nicolosi, F., De Marco, A., Genito, N., and Figliolia, S., "Design of a Low Cost Easy-to-Fly STOL Ultra-Light Aircraft in Composite Material," *Acta Polytechnica*, Vol. 45, No. 4, 2005, pp. 73–80.

[2] Coiro, D. P., Nicolosi, F., Figliolia, S., Grasso, F., De Marco, A., and Genito, N., "Design of a, STOL Ultra-Light Aircraft in Composite Material," *XVIII Congresso Nazionale AIDAA* [CD-ROM], Associazione Italiana Di Aeronautica e Astronautica, Rome, 2005.

[3] Coiro, D. P., Nicolosi, F., De Marco, A., Scherillo, F., and Grasso, F., "High-Lift Systems for STOL Ultra-Light Aircraft, Design and Wind-Tunnel Tests," *XIX Congresso Nazionale AIDAA* [CD-ROM], Associazione Italiana Di Aeronautica e Astronautica, Rome, 2007.

[4] Lin, J. C., and Dominik, C. J., "Parametric Investigation of a High Lift Airfoil at High Reynolds Numbers," *Journal of Aircraft*, Vol. 34, No. 4, July–Aug. 1997, pp. 485–491. doi:10.2514/2.2217

[5] Spaid, F. W., "High Reynolds Number, Multielement Airfoil Flowfield Measurements," *Journal of Aircraft*, Vol. 37, No. 3, May–June, 2000, pp. 499–507. doi:10.2514/2.2626

[6] Moir, I., "Measurements on a Two-Dimensional Airfoil with High Lift Devices: A Selection of Experimental Test Cases for the Validation of CFD Codes," AGARD Rept. AR-303, Neuilly-sur-Seine, France, Aug. 1994.

[7] Balaji, R., Bramkamp, F., Hesse, M., and Ballmann, J., "Effect of Flap and Slat Riggings on 2-D High-Lift Aerodynamics," *Journal of Aircraft*, Vol. 43, No. 5, Sept.–Oct. 2006, pp. 1259–1271. doi:10.2514/1.19391

[8] Grasso, F., "Progetto e Analisi di un Profilo Alare Multicomponente per Applicazioni, S.T.O.L," M.S. Thesis, Univ. Degli Studi di Napoli Federico II, Dipartimento di Ingegneria Aerospaziale, 2005.

[9] Drela, M., "XFOIL User Guide," ver. 6.94, MIT Aero & Astro, Dec. 2001.

[10] Coiro, D. P., and de Nicola, C., "Prediction of Aerodynamic Performance of Airfoils in Low Reynolds Number Flows," *Low Reynolds Number Aerodynamics Conference*, Springer–Verlag, Berlin, 1989.

[11] Coiro, D. P., and Dini, P., "Stall and Post-Stall Performance Prediction of Advanced Wind-Turbine Airfoils," *XII AIDAA Congress* [CD-ROM], Associazione Italiana Di Aeronautica e Astronautica, Rome, 1993.

[12] Coiro, D. P., and Dini, P., "Prediction of Airfoil Stall over Wind-Turbine Airfoils," *FTEC '97 Congress*, Vol. 1, Inst. Teknologi Bandung, Bandung, Indonesia, July 1997, pp. 297–308.

[13] Coiro, D. P., and Nicolosi, F., "Aerodynamics, Dynamics and Performance Prediction of Sailplanes and Light Aircraft," *Technical Soaring*, Vol. 24, No. 2, Apr. 2000, pp. 34–40.

[14] Roskam, J., "Preliminary Sizing of Airplanes," Pts. 1, 2, 4, DARcorporation, Lawrence, KS, 1997.

[15] Besnard, E., Schimtz, A., Boscher, E., Garcia, N., and Cebeci, T., "Two Dimensional Aircraft High Lift System Design and Optimization," AIAA Paper 98-0123, 1998.

[16] Kim, S., Alonso, J. J., and Jameson, A., "Design Optimization of High Lift Configurations Using a Viscous Adjoint-Based Method," *Journal of Aircraft*, Vol. 41, No. 5, Sept.–Oct. 2004, 1082–1097. doi:10.2514/1.17

[17] Egglestone, B., McKinney, W. D., Banaszek, J., Choi, N. S., Krolikowski, G., Lebrun, F., Thompson, J., Zingg, D. W., Nemec, M., and De Rango, S., "Development of a New Flap for a Light Utility Transport Aircraft," *Canadian Aeronautics and Space Journal*, Vol. 48, No. 4, Dec. 2002, pp. 233–238.

[18] Drela, M., "A User's Guide to MSES," Ver. 2.9, Massachusetts Inst. of Technology, Computational Aerospace Sciences Lab., Cambridge, MA, Oct. 1995.

[19] Rae, W. H., and Pope, A., Low Speed Wind Tunnel Testing, 2nd ed., Wiley-Interscience, New York, 1984.